

60

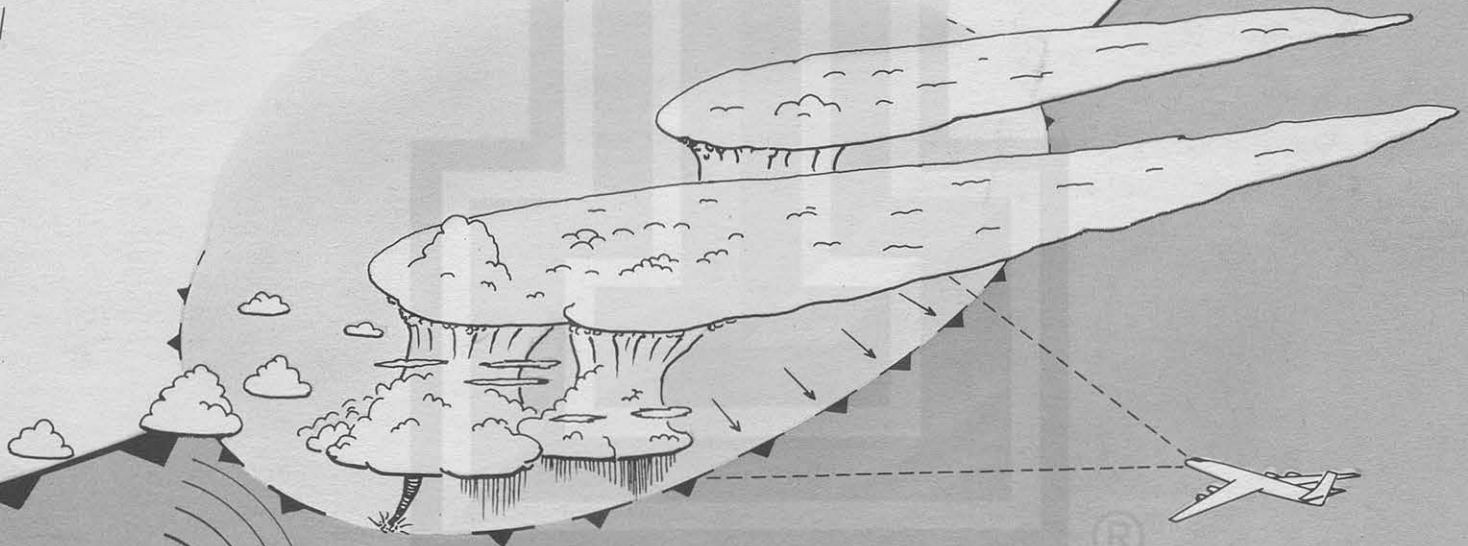
SATELLITE & MESOMETEOROLOGY RESEARCH PROJECT

*Department of the Geophysical Sciences
The University of Chicago*

A MODEL OF TYPHOONS ACCOMPANIED BY INNER
AND OUTER RAINBANDS

Tetsuya Fujita and Tatsuo Izawa
The University of Chicago, U. S. A.

Kazuo Watanabe and Ichiro Imai
Meteorological Research Institute, Japan



SMRP Research Paper

NUMBER 60

March 1966

MESOMETEOROLOGY PROJECT --- RESEARCH PAPERS

- 1.* Report on the Chicago Tornado of March 4, 1961 - Rodger A. Brown and Tetsuya Fujita
- 2.* Index to the NSSP Surface Network - Tetsuya Fujita
- 3.* Outline of a Technique for Precise Rectification of Satellite Cloud Photographs - Tetsuya Fujita
- 4.* Horizontal Structure of Mountain Winds - Henry A. Brown
- 5.* An Investigation of Developmental Processes of the Wake Depression Through Excess Pressure Analysis of Nocturnal Showers - Joseph L. Goldman
- 6.* Precipitation in the 1960 Flagstaff Mesometeorological Network - Kenneth A. Styber
- 7.** On a Method of Single- and Dual-Image Photogrammetry of Panoramic Aerial Photographs - Tetsuya Fujita
8. A Review of Researches on Analytical Mesometeorology - Tetsuya Fujita
9. Meteorological Interpretations of Convective Neph systems Appearing in TIROS Cloud Photographs - Tetsuya Fujita, Toshimitsu Ushijima, William A. Hass, and George T. Dellert, Jr.
10. Study of the Development of Prefrontal Squall-Systems Using NSSP Network Data - Joseph L. Goldman
11. Analysis of Selected Aircraft Data from NSSP Operation, 1962 - Tetsuya Fujita
12. Study of a Long Condensation Trail Photographed by TIROS I - Toshimitsu Ushijima
13. A Technique for Precise Analysis of Satellite Data; Volume I - Photogrammetry (Published as MSL Report No. 14) - Tetsuya Fujita
14. Investigation of a Summer Jet Stream Using TIROS and Aerological Data - Kozo Ninomiya
15. Outline of a Theory and Examples for Precise Analysis of Satellite Radiation Data - Tetsuya Fujita
16. Preliminary Result of Analysis of the Cumulonimbus Cloud of April 21, 1961 - Tetsuya Fujita and James Arnold
17. A Technique for Precise Analysis of Satellite Photographs - Tetsuya Fujita
18. Evaluation of Limb Darkening from TIROS III Radiation Data - S.H.H. Larsen, Tetsuya Fujita, and W.L. Fletcher
19. Synoptic Interpretation of TIROS III Measurements of Infrared Radiation - Finn Pedersen and Tetsuya Fujita
20. TIROS III Measurements of Terrestrial Radiation and Reflected and Scattered Solar Radiation - S.H.H. Larsen, Tetsuya Fujita, and W.L. Fletcher
21. On the Low-level Structure of a Squall Line - Henry A. Brown
22. Thunderstorms and the Low-level Jet - William D. Bonner
23. The Mesoanalysis of an Organized Convective System - Henry A. Brown
24. Preliminary Radar and Photogrammetric Study of the Illinois Tornadoes of April 17 and 22, 1963 - Joseph L. Goldman and Tetsuya Fujita
25. Use of TIROS Pictures for Studies of the Internal Structure of Tropical Storms - Tetsuya Fujita with Rectified Pictures from TIROS I Orbit 125, R/O 128 - Toshimitsu Ushijima
26. An Experiment in the Determination of Geostrophic and Isalobaric Winds from NSSP Pressure Data - William Bonner
27. Proposed Mechanism of Hook Echo Formation - Tetsuya Fujita with a Preliminary Mesosynoptic Analysis of Tornado Cyclone Case of May 26, 1963 - Tetsuya Fujita and Robbi Stuhmer
28. The Decaying Stage of Hurricane Anna of July 1961 as Portrayed by TIROS Cloud Photographs and Infrared Radiation from the Top of the Storm - Tetsuya Fujita and James Arnold
29. A Technique for Precise Analysis of Satellite Data, Volume II - Radiation Analysis, Section 6. Fixed-Position Scanning - Tetsuya Fujita
30. Evaluation of Errors in the Graphical Rectification of Satellite Photographs - Tetsuya Fujita
31. Tables of Scan Nadir and Horizontal Angles - William D. Bonner
32. A Simplified Grid Technique for Determining Scan Lines Generated by the TIROS Scanning Radiometer - James E. Arnold
33. A Study of Cumulus Clouds over the Flagstaff Research Network with the Use of U-2 Photographs - Dorothy L. Bradbury and Tetsuya Fujita
34. The Scanning Printer and Its Application to Detailed Analysis of Satellite Radiation Data - Tetsuya Fujita
35. Synoptic Study of Cold Air Outbreak over the Mediterranean using Satellite Photographs and Radiation Data - Aasmund Rabbe and Tetsuya Fujita
36. Accurate Calibration of Doppler Winds for their use in the Computation of Mesoscale Wind Fields - Tetsuya Fujita
37. Proposed Operation of Instrumented Aircraft for Research on Moisture Fronts and Wake Depressions - Tetsuya Fujita and Dorothy L. Bradbury
38. Statistical and Kinematical Properties of the Low-level Jet Stream - William D. Bonner
39. The Illinois Tornadoes of 17 and 22 April 1963 - Joseph L. Goldman
40. Resolution of the Nimbus High Resolution Infrared Radiometer - Tetsuya Fujita and William R. Bandede
41. On the Determination of the Exchange Coefficients in Convective Clouds - Rodger A. Brown

* Out of Print

** To be published

(Continued on back cover)

SATELLITE AND MESOMETEOROLOGY RESEARCH PROJECT

Department of the Geophysical Sciences
The University of Chicago

A MODEL OF TYPHOONS ACCOMPANIED BY INNER
AND OUTER RAINBANDS

by

Tetsuya Fujita and Tatsuo Izawa
The University of Chicago, U.S.A.

Kazuo Watanabe and Ichiro Imai
Meteorological Research Institute, Japan

SMRP Research Paper #60
March 1966

The research reported in this paper has been sponsored by the Meteorological Satellite Laboratory under Grant Cwb WBG-34 and by the U.S. -Japan Cooperative Science Program under Grants NSG GF-179 and JSPS GEO-4. It was also partially supported by the National Hurricane Research Laboratory under Grant Cwb WBG-70.

A MODEL OF TYPHOONS ACCOMPANIED BY INNER
AND OUTER RAINBANDS¹

Tetsuya Fujita and Tatsuo Izawa
The University of Chicago, U.S.A.

Kazuo Watanabe and Ichiro Imai
Meteorological Research Institute, Japan

ABSTRACT

Both hurricanes and typhoons are relatively circular storms with their winds at high levels blowing mostly outward. Assuming that the outflow is characterized by central motion under the influence of the pressure-gradient forces pointing toward the storm center, the absolute angular momentum of the outflow winds and radar echoes were computed. The upward motion inside these echoes plays an important role in the upward transport of the low-level angular momentum. Detailed analysis made by using satellite, radar, and aerological data revealed that the absolute angular momentum of radar echoes near the eye wall is almost one order of magnitude smaller than that of the echoes in the outer rainbands. This fact leads to a suspicion that the radial distribution of the vertical velocity inside a storm would significantly alter the pattern of the outflow winds near the storm top. A numerical model, including the radial distribution of the vertical velocity, was thus established. Computations indicated that the vertical transport of momentum by outer rainbands alters the outflow wind pattern, resulting in the formation of a ring of high-cloud-free region which separates the inner cirrus shield from the outer cirrus decks. This ring sometimes appears as a clear area on a satellite photograph.

¹The research reported in this paper has been sponsored by the Meteorological Satellite Laboratory under Grant Cwb WBG-34 and by the U.S. -Japan Cooperative Science Program under Grants NSF GF-179 and JSPS GEO-4. It was also partially supported by the National Hurricane Research Laboratory under Grant Cwb WBG-70.

1. Introduction

Typhoons and hurricanes are the names given to the violent tropical storms developing over the Pacific and Atlantic Oceans, respectively. Even though these storms are quite similar in nature, typhoons occasionally develop into huge, violent storms. Taking into consideration the excellent radar, upper-air network, and TIROS photographic and radiation data coverage, Typhoon Bess of August 1963, which moved over western Japan, was chosen for intensive research.

In the past, study of individual tropical cyclones was hampered by a limited number of observations. To overcome this difficulty, Hughs (1952), Jordan (1952), Miller (1958), and Izawa (1964) attempted to construct composite maps representing the structure of a mean storm.

With the beginning of research flights through hurricanes by the National Hurricane Research Laboratory, studies of individual storms have become feasible. Research on Hurricane Daisy of 1958 by Riehl and Malkus (1961) and Malkus, Ronne, and Chaffee (1961) and on Hurricane Helene of 1958 by Miller (1962) contributed a great deal to the understanding of individual storms.

Development of weather radar for use in meteorology provided a method of indirect sensing of the precipitation patterns usually appearing as hurricane rainbands, first studied comprehensively by Wexler (1947). Ligda (1955) found later that the rainbands can be classified into inner and outer rainbands according to their appearance and formation processes, which are closely related to the distance from the storm center. Ligda also found that the wind velocity can be estimated from the movement of a small precipitation area. Despite the fact that radar is a powerful tool for detecting precipitation in a storm, its use in the study of hurricane outflow is quite restricted.

A difference of about 180° in the directions of motion of low and high clouds over the region of an approaching typhoon has long been observed, even before a radiosonde was first used in meteorology. Attracted by such a large difference in cloud motion, Ishimaru (1924) carefully observed the movement of high clouds during the passage of the Okinawa typhoon of 1924, finding anticyclonic outflow of cirrus clouds at about 500 km and 1000 km from the storm center.

The TIROS meteorological satellites dating back to April 1960, have shown their potential value in hurricane research. Of a large number of studies of hurricanes and typhoons made by using satellite photographs, Fett's (1964) model of tropical cyclones, including the outflow shear line and the annular clear region surrounding the cirrus shield,

explains various features of such storms seen in satellite pictures. A quantitative estimate of the wind speed of tropical storms and cyclones was devised by Timchalk, Hubert, and Fritz (1965). In their method, the size of the cirrus shield and the degree of spiral organization are related empirically to the intensity of the storms.

2. Radiative and Photographic Characteristics of Inner Cirrus Shield and Outer Cirrus Decks

Typhoon Bess of August 1963 intensified very rapidly on the 3rd, when its central pressure dropped to 980 mb. After reaching a minimum pressure of 930 mb two days later, a slight filling took place; however, its central pressure was maintained between 950 and 960 until the 8th, when the storm reached 100 km to the southeast of Kyushu, Japan. Figure 1 shows the path of the typhoon center as well as its central pressure. The painted circles indicate radiosonde stations identified with the International Station Numbers.

Used in the study of the typhoon structure are TIROS VII data from Orbits 721 (Aug. 7) and 736 (Aug. 8) during which tape-mode photographs were taken successively toward the direction of arrows representing the principal lines. Radiation data are available only from Orbit 736 with a minimum nadir angle of 14° , resulting in closed-mode scanning when radiation from the typhoon area was measured.

A gridded picture, Frame 23T, Orbit 721 exposed at 0428.1Z, Aug. 7, is presented in Fig. 2. A well-defined eye about 100 km in diameter is clearly visible. When the pattern of outflowing cirrus is examined, it is found that a relatively thick cirrostratus covers the inner portion of the storm whereas the outer portion is characterized by locally thick cirrus clouds which are closely related to the distribution of convective cells forming the outer rainbands.

About 24 hours later the satellite in Orbit 736 obtained oblique pictures of the storm. A gridded picture, Frame 20T exposed at 0451.4Z, Aug. 8, presents the outer boundary of the cirrostratus covering the inner portion of the storm (Fig. 3). This boundary extends to the northeast from southern Kyushu to 33N and 132E, then eastward to 33N and 135E. The cirrus clouds outside this boundary became thicker during the preceding 24 hours, reaching the southern tip of Korea. Cirrus streaks, both in the directions parallel and perpendicular to the vertical wind shear, are visible over the Korea Strait between Japan and Korea.

It should be pointed out that the pattern of cirrus at the outflow level is characterized by a solid cirrus shield over the inner storm area and by streaks and

patches of cirrus over the outer regions. These cirrus clouds are identified in this paper as the "inner cirrus shield" and the "outer cirrus decks," respectively. These terms are closely related to the structure of hurricanes studied by Fett (1964), who pointed out that outer convective bands or pre-hurricane squall lines partially ring the storm and that the hurricane cirrus shield is surrounded totally or partially by an annular zone that is relatively cloud free.

Although the scanning radiometers of TIROS satellites do not resolve temperatures of individual cloud systems seen in a satellite picture, the radiation patterns mapped from the radiation data permit us to evaluate radiative characteristics of the nephosystems quantitatively. In order not to lose the resolution through mapping processes, original analog traces were reduced by using SMRP's scanning printer designed by Fujita (1965), and the radiation patterns were transferred to the satellite picture of Fig. 3.

The effective radiant emittance of Channel 2, the 8-12 micron window channel, is contoured in Fig. 4. The limb darkening should be very small since the nadir angle of scan was less than 50° and the scanning was made entirely in the closed mode. The equivalent blackbody temperature of the reported cloud-free area west of Korea was 9C, about 16C colder than the actual sea-surface temperature. This difference is probably due to the atmospheric absorption by a "dirty" window. At the cirrus-top level, this absorption would be negligibly small, permitting us to consider that the equivalent blackbody temperatures from the scan spots, including solid cirriform cloud with 1.0 emissivity, represent the cloud-top temperatures. The black circles in the figure indicate these scan spots. Their temperature ranges between -27C and -45C, corresponding, respectively, to the 300- and 200-mb temperatures over Kyushu. Radiation patterns, as well as its appearance in the picture, reveal that a cloud mass near the southern tip of Korea is not a high cloud. The equivalent blackbody temperature of streaky cirrus over the Korea Strait is quite low, despite its faint appearance.

The reflectance of this streaky cirrus was between 30 and 50%, which is relatively high in comparison with the 73% reflectance of the thick cirrostratus forming the inner cirrus shield (Fig. 5). The reflectance contours were obtained from Channel 3 data, including the spectral range between 0.3 and 4 microns. Even though the cloud mass over Korea seems quite bright in the satellite photograph, the Channel 3 reflectance was only 50%, which is no more than that of the faint streaky cirrus over the Korea Strait.

The reflectance under discussion is the so-called "planetary reflectance" which includes both the cloud reflectance and the attenuation due to the atmosphere above the cloud top. Fujita and Grandoso (1966) derived an equation for computing the cloud reflectance, \bar{R}_s , from the measured planetary reflectance, \bar{R}_c , and Channel 2 radiation data. This equation is

$$\bar{R}_s = \bar{R}_c (1 - k a_0 \bar{W}_c / \bar{W}_b)^{-1}, \quad (1)$$

where \bar{W}_c and \bar{W}_b are the Channel 2 effective radiant emittance of the clouds and the background, respectively; k , a constant which is about 0.6; and a_0 , the extinction coefficient at sea level, which varies with the solar and satellite zenith angles. The reflectances shown near the black circles in Fig. 5 are the cloud reflectances, \bar{R}_s , computed by Eq. (1). These values indicate that the outer cirrus decks are as reflective as the inner cirrus shield when they are rather thick. Note that the northwestern boundary of the inner cirrus shield extends from southern Kyushu to south of Shikoku.

Fujita and Grandoso's (1966) method of combining short- and long-wave radiation data permits us to compute the whiteness of high, faint clouds. The whiteness, defined as

$$\beta = n_w / n_B, \quad (2)$$

which is the ratio of the equivalent white cloud cover and the equivalent blackbody cloud cover, and it can be computed from measured radiation data. For the details of the method one should refer to the original article. The results of its application to the radiative characteristics of typhoon cirrus, however, are discussed herein.

Figure 6 includes the equivalent blackbody cloud temperatures at one-degree geographic grid points wherever the whiteness is 1.0, which occurs when individual clouds are highly reflective. Over the region of faint cirrus streaks inside the outer cirrus decks, the whiteness was smaller than 1.0, with computed values as low as 0.42. When the whiteness is very small, the image of a cloud on a photograph appears gray and faint, but it radiates as a blackbody more effectively than its photographic image implies. It is assumed that a cloud with little whiteness is very thin and/or of very large ice-crystals, which are not too reflective but radiate considerably. The fact that the outer cirrus decks in Fig. 6 show relatively low whiteness would indicate that these decks are relatively thin and/or that their constituent ice-crystals are quite large.

The annular distribution of low whiteness of clouds is of extreme interest in relation to the outflow structure of a typhoon or a hurricane.

3. Motion of Radar Echoes and Estimated Absolute Angular Momentum

The absolute angular momentum budget inside tropical cyclones is very important in the study of both the structure and development of storms. Due to the scarcity of upper-air data obtained inside a specific storm, the absolute angular momentum budget was computed by Palmen and Riehl (1957), using a mean wind distribution obtained by Hughes (1952) and Jordan (1952).

Since "zero Doppler winds" were obtained by the APN-82 Doppler wind system on board the U.S. Weather Bureau's DC-6 instrumented aircraft flying through hurricane eye walls, their meteorological meaning has been questioned by hurricane researchers. In their recent study of the effects of wet Doppler beams upon measured winds, Fujita, Black and Loesch (1966) concluded that the zero Doppler winds are the result of heavy precipitation inside a rainband in which four Doppler beams are completely wet, thus locking onto the falling raindrops without receiving signals from the sea surface. The horizontal component of the raindrops should be equal to the horizontal wind velocity in order to measure the zero Doppler winds, even though the vertical motion of the raindrops does not affect the Doppler winds so long as it affects four beams uniformly. Research on the Doppler wet beams leads to an important conclusion that the horizontal velocities of both raindrops and their environmental air are identical. In other words, the angular momentums per unit mass of raindrops and the air are equal or extremely close to each other.

This discussion of basic problems justifies the computation of the absolute angular momentum of a typhoon circulation from the displacement vectors of small radar echoes. The echo velocities given by regular wind symbols in Fig. 7 were computed from three radar pictures taken at about 10-min intervals. The time of this velocity computation was selected to coincide with the exposure time of the satellite picture in Fig. 2, thus allowing superimposition of radar echoes (stippled area) and cloud areas depicted with two gray-scale contours determined from satellite pictures.

The echo motions and the satellite picture are more effectively related in Fig. 8, in which black radar echoes accompanied by their SPA winds as defined by Ligda (1953) are photographically superimposed upon the cloud picture. The one-deg grids of longitude and latitude reveal the locations and dimensions of the nephsystem. Of interest

is the peculiar motion of the echoes inside the box bounded by 31N, 32N, 133E, and 135E. Most of the echoes were moving outward with about a 30° angle with respect to the direction of the environmental echoes and with a speed 10 to 15 kt faster than that of the environmental echoes. The leading edge of the echoes, forming a crescent shape, is located along the front of high winds which deviate considerably from the cyclostrophic winds around the storm center. Significant outer cirrus decks are seen over the region of these fast-moving echoes.

Twenty-four hours later the leading edge of the inner cirrus shield reached southern Kyushu and Shikoku, and the inner rainbands became clearly visible on the Muroto radarscope (Figs. 9 and 10). As has already been pointed out by many radar meteorologists, inner rainbands are characterized by smooth spiral bands, while outer rainbands consist of more distinct cells of echoes somewhat like squall lines. The typhoon center, which was then moving northeastward at 6.5 kt, was located 200 km beyond the maximum range of the Muroto radar.

In order to obtain the tangential velocities of the echoes, the translational velocity of the storm center was first subtracted, then the tangential component of each velocity was obtained by drawing the position vector connecting the echo with the storm center. When these tangential velocities were plotted on tangential speed vs radius diagrams, as in Fig. 11, the absolute angular momentum of the echoes could be immediately be obtained by drawing in the figure the isolines of

$$m = vr + \frac{1}{2} fr^2 \quad (3)$$

where m denotes the absolute angular momentum per unit mass of a radar echo; v , the tangential velocity relative to the storm center; f , the Coriolis parameter; and r , the distance of the echo from the storm center. It is evident that the absolute angular momentum at the 600-km radius from the center is more than $20 \times 10^6 \text{ m}^2 \text{ sec}^{-1}$, while that around the eye wall, estimated from Fig. 11, was only 2 or $3 \times 10^6 \text{ m}^2 \text{ sec}^{-1}$, about one order of magnitude smaller than the former. This is a natural consequence of the winds inside a large circular vortex in which the low-level air converging into the rainbands loses its absolute angular momentum during its long journey from the outermost regions of the storm inward along spirals with rather small crossing angles.

4. Vertical and Radial Transport of Absolute Angular Momentum at the Outflow Level

Since our present problem is limited to the interpretation of the cirrus outflow

as viewed from a meteorological satellite, it is assumed that the upward transport of absolute angular momentum is accomplished only inside the inner and the outer rainbands. Due to the restricted resolution of winds aloft available for a given time and storm, it is not feasible to establish the sink and source of the absolute angular momentum on such multi-layer upper-air charts as shown in Fig. 12. The figure includes the isolines of absolute angular momentum in the unit of $10^6 \text{ m}^2 \text{ sec}^{-1}$. The regions with less than 5×10^6 are hatched and those between 10 and 15×10^6 are stippled. When these regions are compared with the area of the inner cirrus shield, the absolute angular momentum at 200 mb inside the inner cirrus shield is known to be less than 5×10^6 , strongly suggesting that such a small absolute angular momentum originated in the inner rainbands. A small hatched circle on the 600-mb chart represents the area with absolute angular momentum less than 5×10^6 , and the hot towers inside this area would be qualified as the source of small angular momentum.

A search for the source of high absolute angular momentum characterizing the 200-mb winds in the outer regions ends up with a zone at 600 mb near the leading edge of the inner cirrus shield. In other words, a large absolute angular momentum transported upward by the echoes located near the edge of the inner cirrus shield is required to explain the outflow wind field in the regions of the outer cirrus decks. We may thus assume that the source of absolute angular momentum inside the inner cirrus shield and the outer cirrus decks is different. That of the former is from the inner rainbands and of the latter, from the outer rainbands.

A vertical cross-section of absolute angular momentum can be made from a series of upper-air observations taken at a station located on or close to the path of the center of a steady-state storm. The center of Typhoon Bess passed near Fukuoka (807) on Aug. 9 when the storm had been weakening for three days. Nevertheless, a time cross-section from Fukuoka converted into a space cross-section through the storm center revealed a reasonable distribution of the absolute angular momentum in the radial, vertical plane with an azimuth of 330° (Fig. 13). If we assume that this space cross-section represents the case of a steady-state typhoon approaching Fukuoka and that the absolute angular momentum is conserved throughout inflow and outflow processes, except near the surface, the isolines of the absolute angular momentum would represent streamlines in a radial, vertical plane. The figure thus implies that the absolute angular momentum transported upward inside the inner rainbands remains inside the region of the inner cirrus shield while the outflow from the outer rainbands spreads outward through the region of outer cirrus decks.

So far the discussion in this paper has been based upon the assumption that the upward transport of absolute angular momentum takes place mainly inside the inner and outer rainbands. This assumption can be justified if we are able to obtain winds at the outflow level which are dense enough to determine divergence fields associated with these rainbands. Figure 14 was prepared to illustrate an insignificant but existing divergence field over the rainband areas. It will be noticed that a time-to-space conversion technique was used to increase wind data in the rainband areas. Such a wind field can best be depicted by using Doppler winds after correcting errors due to wet-beam effects. At the present time such effects are under intensive joint study by SMRP, University of Chicago and RFF, Environmental Science Services Administration to enable accurate determination of Doppler winds near the top of heavy precipitation areas.

5. An Outflow Model of Typhoons and Hurricanes Accompanied by Inner and Outer Rainbands

We shall now determine the outflow wind field of typhoons and hurricanes in which the rain areas form rainbands. Actual rainbands are characterized by certain crossing angles, thus forming spiral rainbands. To avoid complication of mathematical treatment, all rainbands are approximated as concentric rings surrounding the storm center.

Figure 15 shows a model of the outflow with a constant thickness, h , which receives additional mass supplied from below while the outflowing air is passing over a rainband. Expressing the radial, tangential, and vertical velocities inside the outflow at the radial distance, r , from the center with u , v , and w , respectively, we write the equation of continuity as

$$2\pi r h u + 2\pi r w dr = 2\pi h (r + dr)(u + du),$$

in which ρ , the air density at the outflow level, is assumed constant. Then we write

$$\frac{du}{dr} + \frac{1}{r} u = \frac{w}{h}. \quad (4)$$

This differential equation can at once be integrated after multiplying both sides by r , the integrating factor. Thus we have

$$u = \frac{1}{hr} \int_{r_e}^r r w dr, \quad (5)$$

where r_e denotes the radius of the eye wall at which the radial velocity is zero or $u = 0$.

When a storm is accompanied by both inner and outer rainbands extending from r_i to R_i and from r_o to R_o , respectively, Eq. (5) can be integrated in sections. Then we assume that the vertical velocities at the bottom of the outflow layer are constants, \bar{w}_i for the inner and \bar{w}_o for the outer, to obtain

$$u = \frac{\bar{w}_i}{2hr} (r^2 - r_i^2) \quad \text{when } R_i > r > r_i, \quad (6)$$

$$u = \frac{\bar{w}_i}{2hr} (R_i^2 - r_i^2) \quad \text{when } r_o > r > R_i, \quad (7)$$

$$u = \frac{1}{2hr} \left\{ \bar{w}_i (R_i^2 - r_i^2) + \bar{w}_o (r^2 - r_o^2) \right\} \quad \text{when } R_o < r < r_o, \quad (8)$$

$$u = \frac{1}{2hr} \left\{ \bar{w}_i (R_i^2 - r_i^2) + \bar{w}_o (R_o^2 - r_o^2) \right\} \quad \text{when } R_o < r, \quad (9)$$

These equations permit us to compute the radial velocity at the outflow level when the inside and outside radii of the rainbands and their mean vertical velocities are known.

These equations are also applicable to cases where the vertical velocities inside the rainbands vary as a function of the radius. In such cases the empirical values of w are used to compute

$$\begin{aligned} u &= \frac{1}{2hr_{n+1}} \left\{ \bar{w}_1 (r_2^2 - r_1^2) + \bar{w}_2 (r_3^2 - r_2^2) + \dots + \bar{w}_n (r_{n+1}^2 - r_n^2) \right\} \\ &= \frac{1}{2hr_{n+1}} \sum_1^n \bar{w}_n (r_{n+1}^2 - r_n^2), \end{aligned} \quad (10)$$

where w_n represents the mean vertical velocity between radii r_n and r_{n+1} .

The absolute angular momentum, M , at the outflow level defined as

$$M = rv + \frac{1}{2} fr^2,$$

is computed from the radial distribution of w and m , the absolute angular momentum of the radar echoes inside the rainbands. From the conservation of momentum, we write

$$2\pi rhuM + 2\pi rwm dr = 2\pi h(r+dr)(u+du)(M+dM),$$

which can be reduced to

$$\frac{dM}{dr} + \frac{w}{hu} M = \frac{w}{hu} m. \quad (11)$$

In order to solve this equation we must know both w and u as functions of the radius. The model of the rainbands leading to the solution of Eq. (6) through (9) is now used to solve Eq. (11) in the forms

$$\frac{dM}{dr} + \frac{2r}{r^2 - r_i^2} M = \frac{2r}{r^2 - r_i^2} m_i \quad \text{when } R_i > r > r_i, \quad (12)$$

$$\frac{dM}{dr} = 0 \quad \text{or } M = \text{const.} \quad \text{when } r_0 > r > R_i, \quad (13)$$

$$\frac{dM}{dr} + \frac{2w_0 r}{I} M = \frac{2w_0 r}{I} m_0 \quad \text{when } R_0 > r > r_0, \quad (14)$$

where $I = \bar{w}_i (R_i^2 - r_i^2) + \bar{w}_0 (r^2 - r_0^2),$

$$\frac{dM}{dr} = 0 \quad \text{or } M = \text{const.} \quad \text{when } r > R_0 \quad (15)$$

where m_i and m_0 are the absolute angular momentums of the echoes inside the inner and outer rainbands, respectively. Each may vary as a function of the radius inside the rainband. Thus we solve Eq. (12) as

$$\begin{aligned} M &= \frac{1}{r^2 - r_i^2} \int_{r_i}^r m_i d(r^2) && \text{when } R_i > r > r_i, \\ &= \bar{m}_i && \text{when } m_i \text{ is constant.} \end{aligned} \quad (16)$$

Inside the rain-free area between the inner and outer rainbands the momentum from Eq. (13) should be a constant expressed by

$$M = \frac{I}{R_i^2 - r_i^2} \int_{r_i}^{R_i} \bar{m}_i d(r^2) \quad \text{when } r_0 > r > R_i$$

$$= \bar{m}_i \quad \text{when } \bar{m}_i \text{ is constant.} \quad (17)$$

Next we integrate Eq. (14) after multiplying the integrating factor I, thus

$$[MI]_{r_0}^r = \int_{r_0}^r 2 \bar{w}_0 \bar{m}_0 r dr \quad \text{when } R_0 > r > r_0. \quad (18)$$

If \bar{m}_i and \bar{m}_0 are constants within each rainband, Eq. (18) can be reduced to

$$M = \frac{\bar{m}_i \bar{w}_i (R_i^2 - r_i^2) + \bar{m}_0 \bar{w}_0 (r^2 - r_0^2)}{\bar{w}_i (R_i^2 - r_i^2) + \bar{w}_0 (r^2 - r_0^2)}. \quad (19)$$

It is obvious that the absolute angular momentum keeps a constant value

$$M = \frac{\bar{m}_i \bar{w}_i (R_i^2 - r_i^2) + \bar{m}_0 \bar{w}_0 (R_0^2 - r_0^2)}{\bar{w}_i (R_i^2 - r_i^2) + \bar{w}_0 (R_0^2 - r_0^2)} \quad (20)$$

when $r > R_0$.

In a similar manner in which Eq. (10) was obtained for computing the radial velocity when w is known empirically, it is feasible to compute the absolute angular momentum at the radius r_{n+1} by

$$M = \frac{\sum_1^n \bar{m}_n \bar{w}_n (r_{n+1}^2 - r_n^2)}{\sum_1^n \bar{w}_n (r_{n+1}^2 - r_n^2)}, \quad (21)$$

where \bar{m}_n and \bar{w}_n represent, respectively, the mean absolute angular momentum and the mean vertical velocity between radii r_n and r_{n+1} .

The equations of radial velocity and absolute angular momentum thus derived permit us to calculate tangential and radial velocities as well as the crossing angles of outflowing winds. We have to estimate, however, the vertical velocity at the outflow level as a function of radius. Very little is known about the quantitative values of the areas of penetrative convection inside tropical storms, which are necessary for a reasonable estimate of the mean vertical velocity. The only reliable results have been reported

by Malkus, Ronne, and Chaffe (1958), who completed the laborious work of mapping hot towers and precipitation areas by using radar and cloud photographs. They found that the areas of penetrative convection in Hurricane Daisy of 1958 were only about 1% of the rain area within a radius less than 370 km on the day of formation. This figure increased to 2.5% on deepening day and 4% on the mature day.

Typhoon Bess of Aug. 7-8, 1963 was in a mature stage with clearly identifiable inner and outer rainbands. From Malkus, Ronne, and Chaffe's results it was estimated that 4% of the inner rainband area between the 50- and 100-km radii consisted of hot towers with 10 m sec^{-1} updraft near the tower top and that 2% of the outer rainband area between the 300- and 400-km radii was filled with hot towers of the same updraft velocity. This results in mean vertical velocities of

$$0.4 \text{ m sec}^{-1} \quad \text{for} \quad 50 \text{ km} = r_i < r < R_i = 100 \text{ km}$$

$$\text{and} \quad 0.2 \text{ m sec}^{-1} \quad \text{for} \quad 300 \text{ km} = r_o < r < R_o = 400 \text{ km}.$$

The absolute angular momentums were assumed to be

$$m_i = 2 \times 10^6 \text{ m}^2 \text{ sec}^{-1} \quad \text{for the inner rainbands}$$

$$\text{and} \quad m_o = 12 \times 10^6 \text{ m}^2 \text{ sec}^{-1} \quad \text{for the outer rainbands}.$$

The thickness of the outflow layer was assumed to be a constant, $h = 2 \text{ km}$. Using these values and Eqs. (6) through (9) and (16) through (20), the parameters in Fig. 16 were computed as a function of radius up to 800 km. In fact, two sets of values were computed under the assumption that a storm is accompanied either by inner and outer rainbands or by inner rainbands only.

If a storm is not accompanied by outer rainbands, the relative tangential velocity changes from cyclonic to anticyclonic at a radius of about 200 km, and thereafter the sense of relative circulation remains anticyclonic. When an outer rainband is added, the anticyclonic wind changes into cyclonic. The change in the radial velocity due to the existence of the outer rainband is also significant. Of interest is the effect of the outer rainband computed from the relative tangential and radial velocities upon the crossing angle of the winds. As shown in the middle diagram in Fig. 16, the wind direction changes over 100° , creating a significant, cyclonic, horizontal wind shear along the innermost radius of the outer rainband. Finally, as for the number of days required for an outflowing parcel to travel from the eye-wall region to the outermost region of the storm, calculation showed that it would take 5 days if a storm is accompanied by an inner rainband only. The existence of the outer rainband cuts down the number of days to 1.5, thus providing an efficient wind system to stimulate outflow from the top

of hurricanes and typhoons.

Presented in Fig. 17 are the outflow winds of a storm with both inner and outer rainbands (left half) and with an inner rainband only. In both cases, the outermost region of the outflow is surrounded by a shear line which may be called the "outer shear line." When an outer rainband also exists, a new shear line, which may be called the "inner shear line," appears along the inside radius of the outer rainband. Due to the strong cyclonic shear along the inner shear line, the line may be broken up into a series of cyclonic mesoscale eddies, resulting in a slight drop in pressure inside the eddies. As a natural consequence of the wind and pressure fields along the inner shear lines in which mesoscale eddies are embedded, upper convergence is generated. Thus the outflow air will be forced to move downward because the air cannot move upward beyond the tropopause. Consequently, the inner cirrus shield dissipates as it approaches the inner shear line. A clear annular zone revealed by Fett (1964) probably corresponds to the region of descending motion along the inner shear line. With the existence of the outer rainbands, the outflow continues through the region of the outer cirrus decks, the development of which results in the intensification of the outflow.

A circulation model of two tropical storms, one with and the other without outer rainbands, is presented in Fig. 18. The right half, showing the case of no outer rainband, consists of streamlines at the cirrus level extending outward all the way to the outer shear line that limits the outflow of the storm as a whole. The left half, on the other hand, represents the effect of the existence of the outer rainband giving rise to the development of the inner shear line along which a strong subsidence takes place. Because of the mesoscale eddies, the inner shear line is located between the leading edge of the inner cirrus shield and the inside boundary of the outer rainband.

The pressure profiles at sea level and at the outflow levels are closely related to the outflow patterns resulting from the distribution of the vertical velocity which transports the low-level angular momentum upward.

5. Solution of Outflow Winds for Typhoons with Generalized Radial Distribution of Rainbands

Since it is now feasible to calculate both radial velocity, u , and absolute angular momentum, M , from given radial distributions of vertical velocity, w , and the absolute angular momentum of the radar echoes, m , an attempt was made to calculate various parameters of outflow winds for various typhoon models.

First, the absolute angular momentum of the rader echoes was obtained from scatter diagrams, shown in Fig. 11, by taking the mean values as a function of the distance from the center. These values were then used in determining the distribution of the momentum of the echoes, shown in Table I, which was used for all model typhoons with differently distributed vertical velocities.

TABLE I. Absolute Angular Momentum of Echoes

Radii	100	200	300	400	500	600	700	km
m	4.0	8.2	12.2	16.2	20.5	24.4	28.5	$\times 10^6 \text{m}^2 \text{sec}^{-1}$
$l/2fr^2$	0.4	1.5	3.3	5.8	9.1	13.1	17.9	$\times 10^6 \text{m}^2 \text{sec}^{-1}$
vr	3.6	6.7	8.9	10.4	11.4	11.3	10.6	$\times 10^6 \text{m}^2 \text{sec}^{-1}$

The vertical velocities were assumed separately for the inner and outer rainbands to obtain various model typhoons through their combinations. Figure 19 presents the vertical velocity distributions A, B, and C for the inner rainbands and D, E, and F for the outer rainbands. The addition of the distribution O, designating no vertical velocity, permits us to obtain 15 model typhoons through simple combinations. These are A-O, A-D, A-E, A-F, B-O, B-D, B-E, B-F, C-O, C-D, C-E, C-F, O-D, O-E, and O-F, where O-O has been omitted because it does not indicate a storm.

It should be noted that the distributions C and F include negative vertical velocity or downward motion which will reduce the mass outflow. The radial velocity can be computed from Eq. (10) without modification by simply putting negative values of w within the ranges of predetermined radii. Computations of M within the radius ranges of negative w cannot be made by using Eq. (21), which is applicable only when w is positive. To solve a case of negative vertical velocity, it is necessary to start from Eq. (11) and integrate the equation after changing m into M , because downward motion subtracts M , instead of m , from the outflowing air. The solution is written simply as

$$\frac{dM}{dr} = 0 \quad \text{or} \quad M = \text{const.}$$

That is, the absolute angular momentum remains unchanged while the outflowing air travels under the influence of downward motion at the bottom of the layers of outflow.

For practical computation purposes we consider a case where \bar{w}_{m-1} is negative between r_{m-1} and r_m , and \bar{w}_m is positive between r_m and r_{m+1} . From Eq. (21) we write

$$M_{(r_{m-1})} = \frac{\sum_{n=1}^{n=m-2} \bar{m}_n \bar{w}_n (r_{n+1}^2 - r_n^2)}{\sum_{n=1}^{n=m-2} \bar{w}_n (r_{n+1}^2 - r_n^2)}, \quad (22)$$

where the denominator is identical to $2 h u r_{m-1}$. The next absolute angular momentum at the radius r_m is identical to $M_{(r_{m-1})}$, but it should be expressed as

$$M_{(r_m)} = \frac{\sum_{n=1}^{n=m-2} \bar{m}_n \bar{w}_n (r_{n+1}^2 - r_n^2) + M_{(r_{m-1})} \bar{w}_{m-1} (r_m^2 - r_{m-1}^2)}{\sum_{n=1}^{n=m-2} \bar{w}_n (r_{n+1}^2 - r_n^2) + \bar{w}_{m-1} (r_m^2 - r_{m-1}^2)} = M_{(r_{m-1})}, \quad (23)$$

where the denominator is identical to $2 h u r_m$. The next absolute angular momentum $M_{(r_{m+1})}$ is now computed from

$$M_{(r_{m+1})} = \frac{\sum_{n=1}^{n=m-2} \bar{m}_n \bar{w}_n (r_{n+1}^2 - r_n^2) + M_{(r_{m-1})} \bar{w}_{m-1} (r_m^2 - r_{m-1}^2) + \bar{m}_m \bar{w}_m (r_{m+1}^2 - r_m^2)}{\sum_{n=1}^{n=m-2} \bar{w}_n (r_{n+1}^2 - r_n^2) + \bar{w}_{m-1} (r_m^2 - r_{m-1}^2) + \bar{w}_m (r_{m+1}^2 - r_m^2)}, \quad (24)$$

where the denominator is identical to $2 h u r_{m+1}$ and \bar{w}_m is positive between r_m and r_{m+1} . Thus we are able to compute the absolute angular momentum regardless of the signs of w as long as the denominator remains a finite positive value.

From the known values of u and M , other parameters can easily be computed. They are v , the relative tangential velocity; α , the crossing angle measured clockwise from the direction of cyclostrophic wind; and V , the wind speed. They are expressed, respectively, by

$$\begin{aligned} v &= (M - \frac{1}{2} f r^2) r^{-1}, \\ \alpha &= \tan^{-1} u/v, \\ V &= (u^2 + v^2)^{\frac{1}{2}}. \end{aligned} \quad (25)$$

The relative vorticity, $\bar{\zeta}_m$, between r_m and r_{m+1} , where \bar{w}_m is positive, can be obtained by

$$\bar{\zeta}_m = \frac{r_{m+1} v_{m+1} - r_m v_m}{\frac{1}{2}(r_{m+1}^2 - r_m^2)} = \frac{2(M_{m+1} - M_m) - f(r_{m+1}^2 - r_m^2)}{r_{m+1}^2 - r_m^2}, \quad (26)$$

where M_m and v_m are the absolute angular momentum and the tangential velocity along the radius r_m . When the vertical motion, \bar{w}_{m-1} , is negative between r_{m-1} and r_m , Eq. (23) indicates that $M_m = M_{m-1}$. The mean relative vorticity between these radii is now expressed simply by

$$\zeta_{m-1} = -f. \quad (27)$$

In order to calculate these parameters as a function of the distance from the storm center, the radius was divided into 10-km intervals. Values up to 800 km from the center were computed by using the 7094 computer at the University of Chicago.

Computed parameters for selected combinations of vertical velocities inside the inner and outer rainbands are presented in Fig. 20. If there are no outer rainbands, as in the case of A + O and C + O, the cyclonic outflow changes to anticyclonic at a radius of about 250 km. Outside this radius, a very strong cyclonic outflow extends all the way to the outer shear line. The existence of outer rainbands with exponential (D) or periodic (F) distribution of vertical velocity modifies the outflow field, producing an annular ring of intense cyclonic vorticity along the inward wall of the rainbands.

If the inner rainband is strong, the vorticity is rather small. When the inner rainband is weak and the outer rainband is strong, however, the annular cyclonic vorticity appears to be very large-- 44×10^{-5} sec. Cyclonic vorticity of this magnitude is comparable to that of a low-pressure system with 20-kt cyclostrophic winds along a 50-km radius.

As a result of the development of an annular ring of cyclonic vorticity, pressure decrease and subsequent upper convergence take place near the inward wall of an outer rainband. Such a field of motion will gradually suppress the updraft near the inward wall, resulting in an outward shifting of the annular updraft. At the same time a descending motion develops along the inward wall of the rainband, giving rise to the dissipation of the clouds. These dynamical processes will cause the outward propagation or expansion of a circular updraft accompanied by a zone of subsidence along the inward wall.

The results of the model experiments revealed that a ring of large cyclonic vorticity develops only if a relatively intense vertical motion is added in the outer region of an existing tropical storm. When the identical vertical motion is added in the inner region, the difference between the absolute angular momentums of rising and outflowing air is so small that no cyclonic vorticity develops at the outflow level. The outer rainband is, therefore, quite different from the inner one in dynamical characteristics, and it propagates outward, leaving an annular ring of relatively clear sky. Since inner rainbands do not propagate outward, well-developed typhoons or hurricanes are accompanied by both inner and outer rainbands which are dynamically different entities.

Conclusions.

Through detailed analysis of TIROS photographs, radiation data, radar pictures, and synoptic data, it was found that a well-developed typhoon is accompanied by inner and outer rainbands. When photographed from TIROS altitudes, the cirriform clouds inside the outflow layer appear as the "inner cirrus shield," covering mostly the region of inner rainbands. The "outer cirrus decks" are seen over the outer rainbands.

Under the assumption that the vertical transport of low-level momentum into the outflow layer is accomplished only inside the inner and outer rainbands, numerical experiments of outflow wind fields were undertaken by changing rainband patterns. The results indicated that a reasonably strong upward motion produces a cyclonic wind field at the outflow level only when such an upward motion is added within the outer region of a storm. The upper convergence induced by the cyclonic vorticity field initiates an outward shifting or expansion of the outer rainbands, resulting in the separation of the inner and outer rainbands.

Additional numerical experiments using a three-layer model will be made in order to establish a more reasonable circulation model of a tropical storm with inner and outer rainbands.

Acknowledgements: The authors are grateful to the staff members of SMRP, the University of Chicago and to the Typhoon Research Laboratory, Meteorological Research Institute, Tokyo for their assistance in the completion of this paper.

REFERENCES

- Fett, R. W., 1964: Aspects of hurricane structure: new model considerations suggested by TIROS and Project Mercury Observations. Mon. Wea. Review, 92, 43-60.
- Fujita, T., P. Black, and A. Loesch, 1966: Influence of wet Doppler beams in the determination of mesoscale wind fields across hurricane rainbands. SMRP Rep. 59.
- Fujita, T. and Hector Grandoso, 1966: A proposed method of estimating cloud-top temperature, cloud covers, and emissivity and whiteness of clouds from short- and long-wave radiation data obtained by TIROS scanning radiometers. SMRP Rep. 48.
- Hughs, L. A., 1952: On the low-level structure of tropical storms. J. Meteor., 9, 422-428.
- Ishimaru, Y., 1924: Upper-cloud observation during the passage of a typhoon. J. Japan Met. Soc., 3, 221-225.
- Izawa, T., 1964: On the mean wind structure of typhoons. Typhoon Research Lab. Tech. Note 2, 47 pp.
- Jordan, E. S., 1952: An observational study of the upper wind structure around tropical storms. J. Meteor., 9, 340-346.
- Ligda, M. G. H., 1953: The horizontal motion of small precipitation areas as observed by radar. M.I.T. Tech. Rep. 21.
- _____, 1955: Analysis of motion of small precipitation areas in the hurricane, August 23-28, 1949. M.I.T. Tech. Note 3.
- Malkus, J., C. Ronne, M. Chaffee, 1961: Cloud patterns in hurricane Daisy, 1958. Tellus 13, 8-30.

Miller, B. I., 1958: The three-dimensional wind structure around a tropical cyclone. NHRP Rep. 15, 41 pp.

_____, 1962: On the momentum and energy balance of Hurricane Helene, 1958. NHRL Rep. 53, 19 pp.

Palmen, E., and H. Riehl, 1957: Budget of angular momentum and energy in tropical cyclone. J. Meteor., 14, 150-159.

Riehl, H. and J. Malkus, 1961: Some aspects of hurricane Daisy, 1958. Tellus XIII, 2, 181-213.

Timchalk, A., L. F. Hubert, and S. Fritz, 1965: Wind speeds from TIROS pictures of storms in tropics. MSL Rep. 33, 33 pp.

Wexler, H., 1947: Structure of hurricanes as determined by radar. Ann. N. Y. Acad. Sci., 48, 821-844.

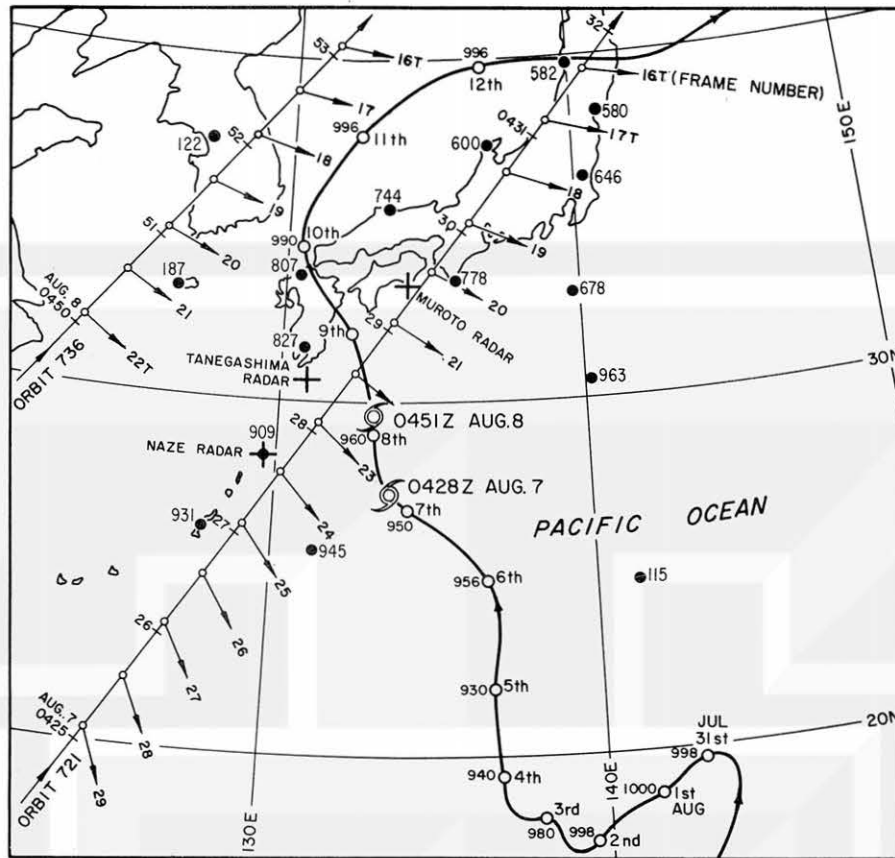


Fig. 1. Path of Typhoon Bess of 1963. Open circles represent daily positions of the storm center at 00 GMT or 09 JMT. Two TIROS VII passes used in this paper and the directions of principal lines are also included. Plus symbols and painted circles represent radar and upper-air stations identified with International Station Numbers.

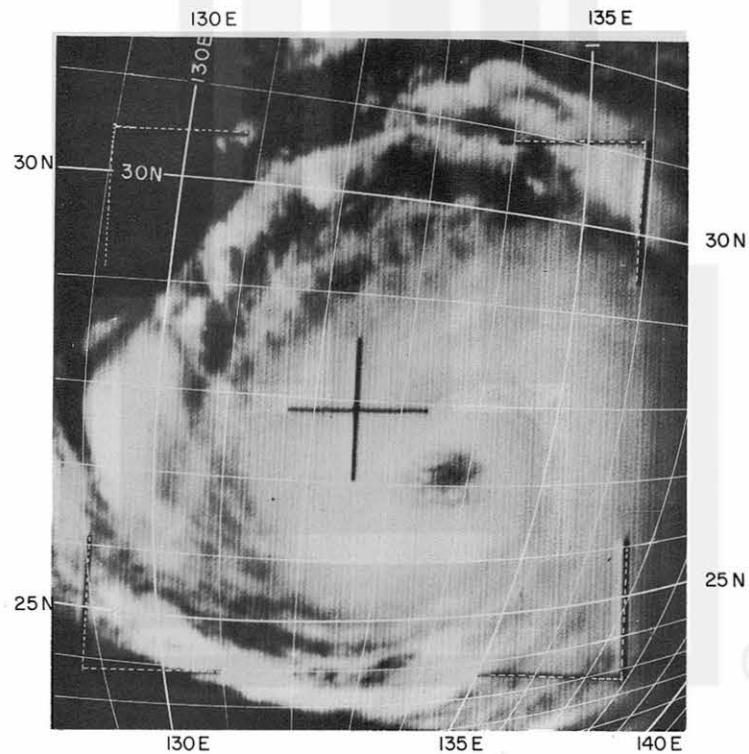


Fig. 2. Typhoon Bess as seen on Frame 23T, Orbit 721, TIROS VII exposed at 0428.1 GMT, Aug. 7, 1963. Photogrammetric data: satellite height, 627 km; exposure sublatitude, 29.3N; sublongitude, 131.4E; tilt, 17.3°; and principal-line azimuth, 132.1°.

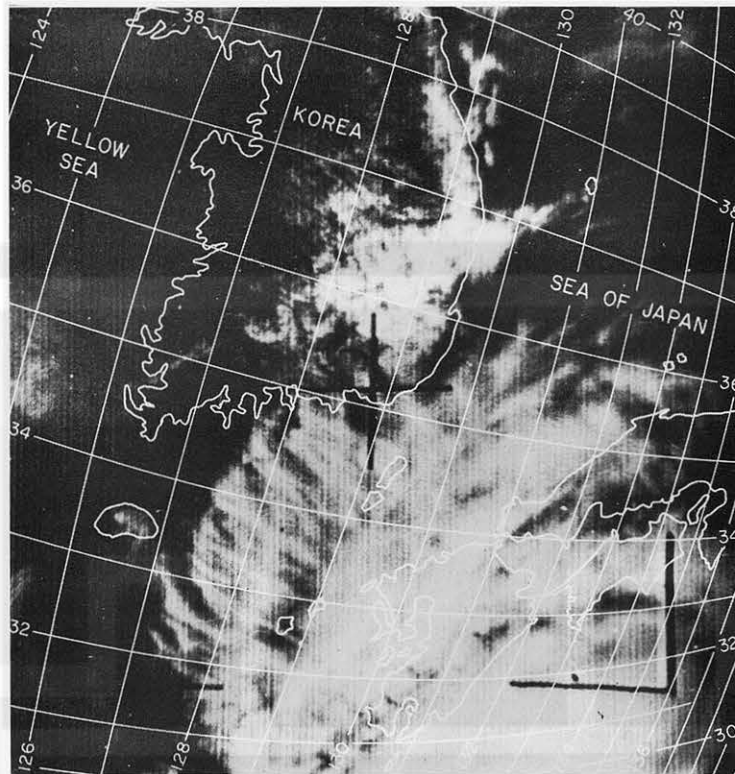


Fig. 3. The inner cirrus shield and the outer cirrus deck of Typhoon Bess appearing in tape-mode picture, Frame 20, Orbit 736, TIROS VII, exposed at 0451.4 GMT, Aug. 8, 1963. Photogrammetric data: satellite height, 627 km; exposure sublatitude, 35.7N; sublongitude, 126.7E; tilt, 15.4°; and principal-line azimuth, 104.0°.

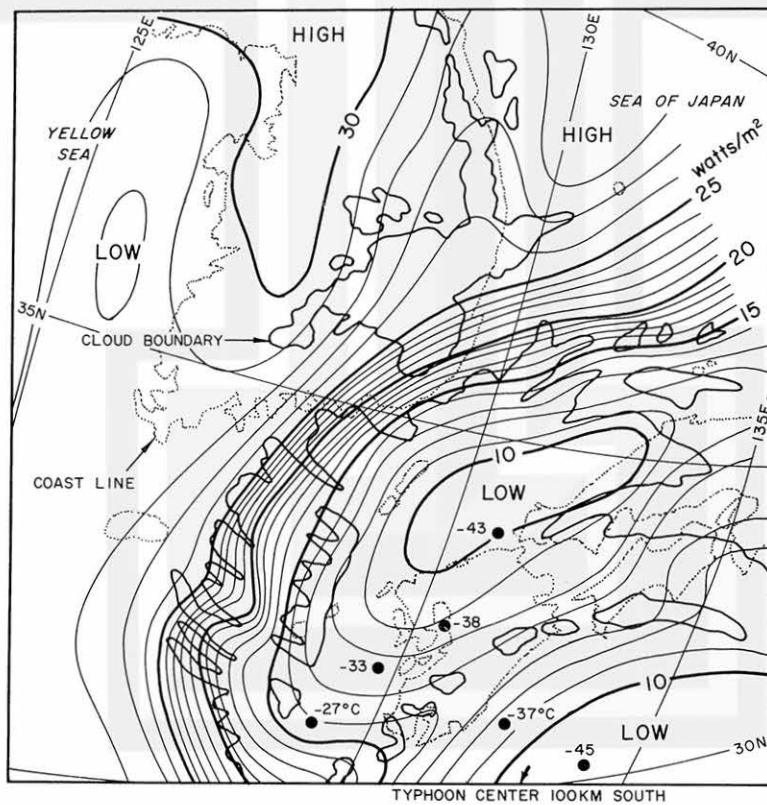


Fig. 4. Channel 2 (8-12 micron) effective radiant emittance measured by TIROS VII on orbit 736 at approximately 0450 GMT Aug. 8, 1963 and drawn on the photographic coordinates of Fig. 3. Temperatures entered near black circles are the equivalent blackbody temperatures obtained from scan spots filled with thick clouds. Calibration data are 30 watts m^{-2} (+11C), 25 (0C), 20 (-11C), 15 (-25C), 19 (-43C).

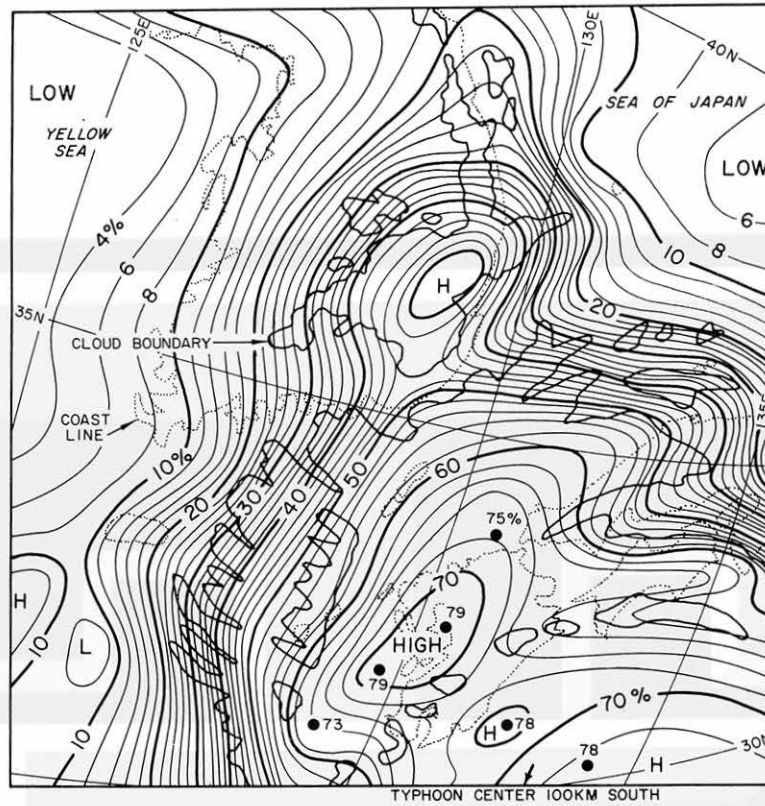


Fig. 5. Channel 3 (0.2-6 micron) reflectance measured by TIROS VII on orbit 736 at approximately 0450 GMT Aug. 8, 1963, contoured on the photographic coordinates of Fig. 3. Values plotted near black circles are the cloud reflectance excluding atmospheric attenuation.

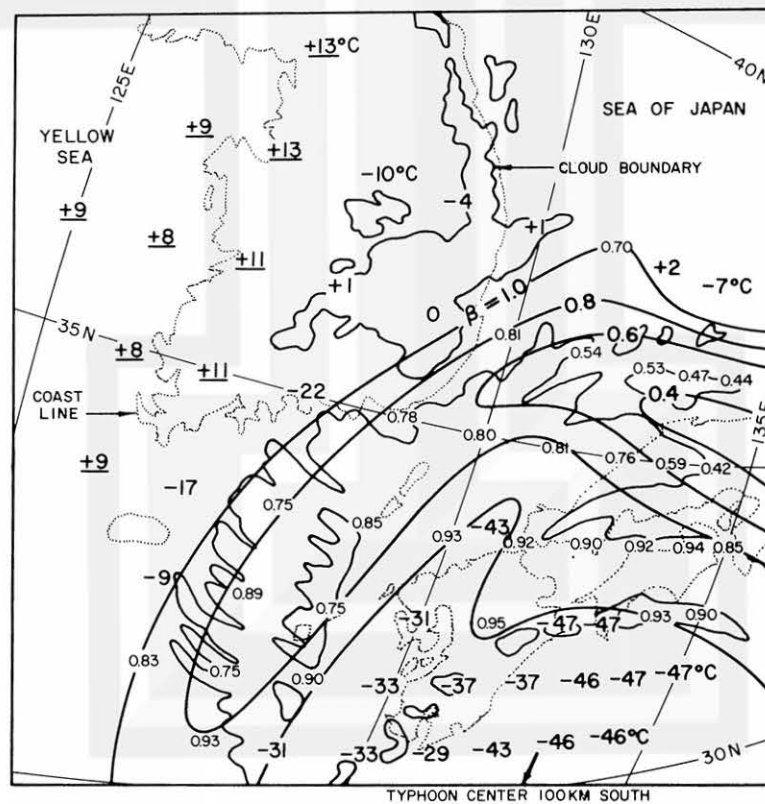


Fig. 6. Equivalent blackbody cloud-top temperatures in bold letters and the whiteness of clouds contoured for every 0.2. Note that the outermost region of the outer cirrus decks is characterized by low values of whiteness. Analyses in Figs. 4 and 5 were combined to obtain this figure.

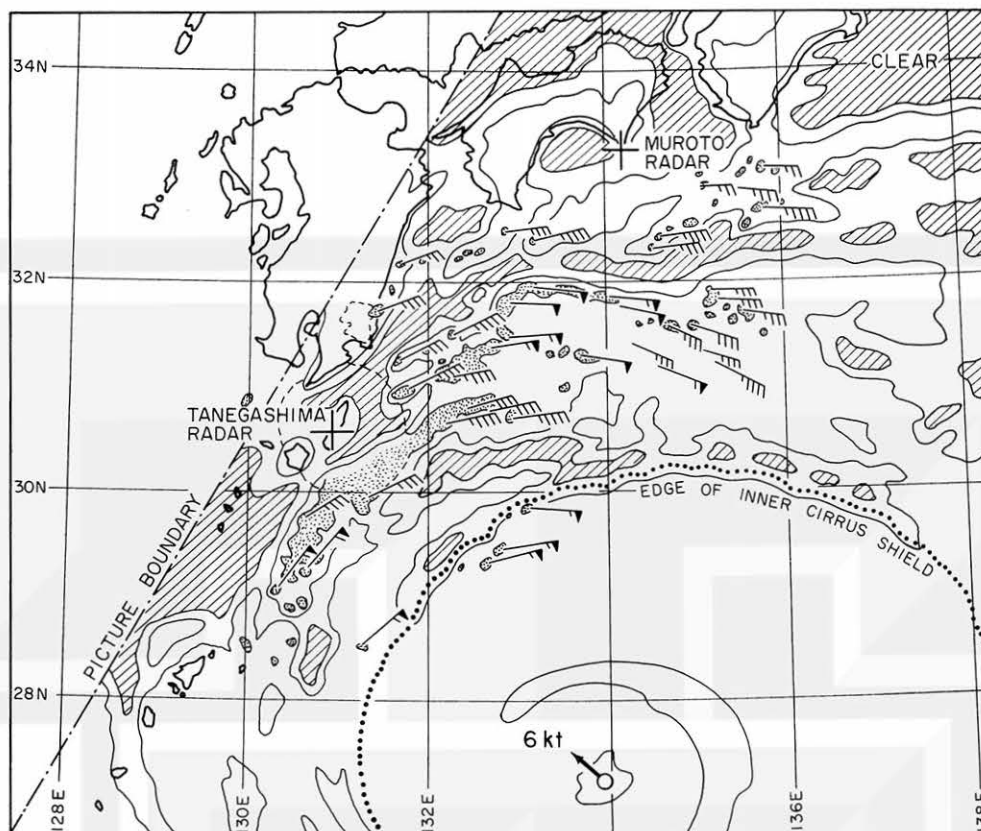


Fig. 7. Radar echoes photographed at Tanegashima at 0430 GMT, Aug. 7, 1963 are indicated by stippled areas and their velocities expressed by regular wind symbols. Rectified satellite cloud patterns are shown by two intensity contours. Clear areas are hatched.

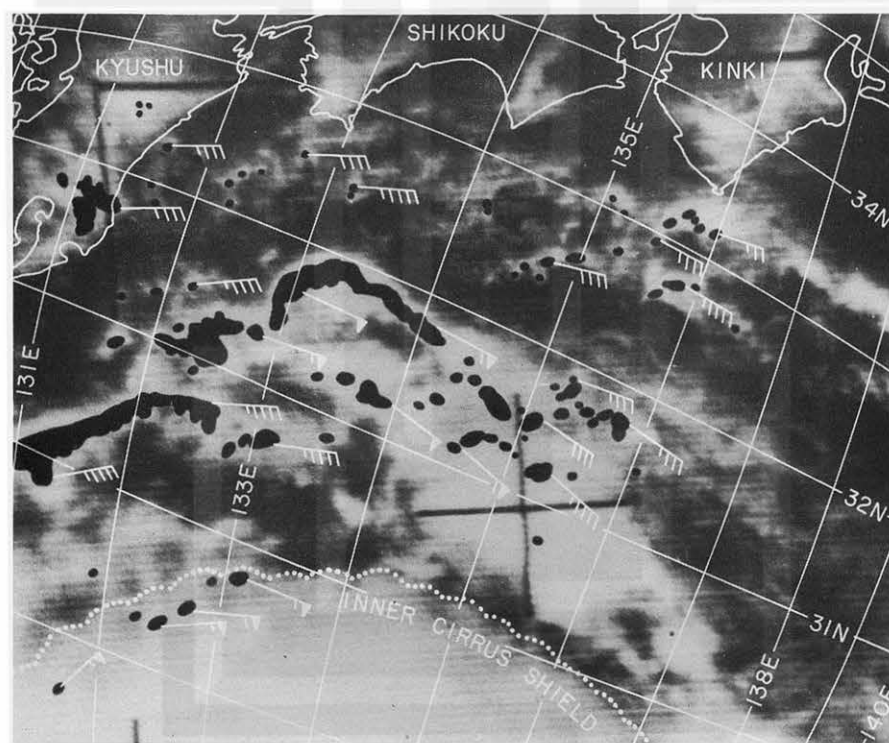


Fig. 8. Radar echoes superimposed upon an enlarged satellite picture gridded with one-deg latitudes and longitudes. An area of high-speed echoes near the center of the figure is covered by a large outer cirrus deck. Note the direction of motion of high-speed echoes, which is about 30° outward compared with the general direction of the echoes in the vicinity. The map is within a few minutes of Fig. 2.

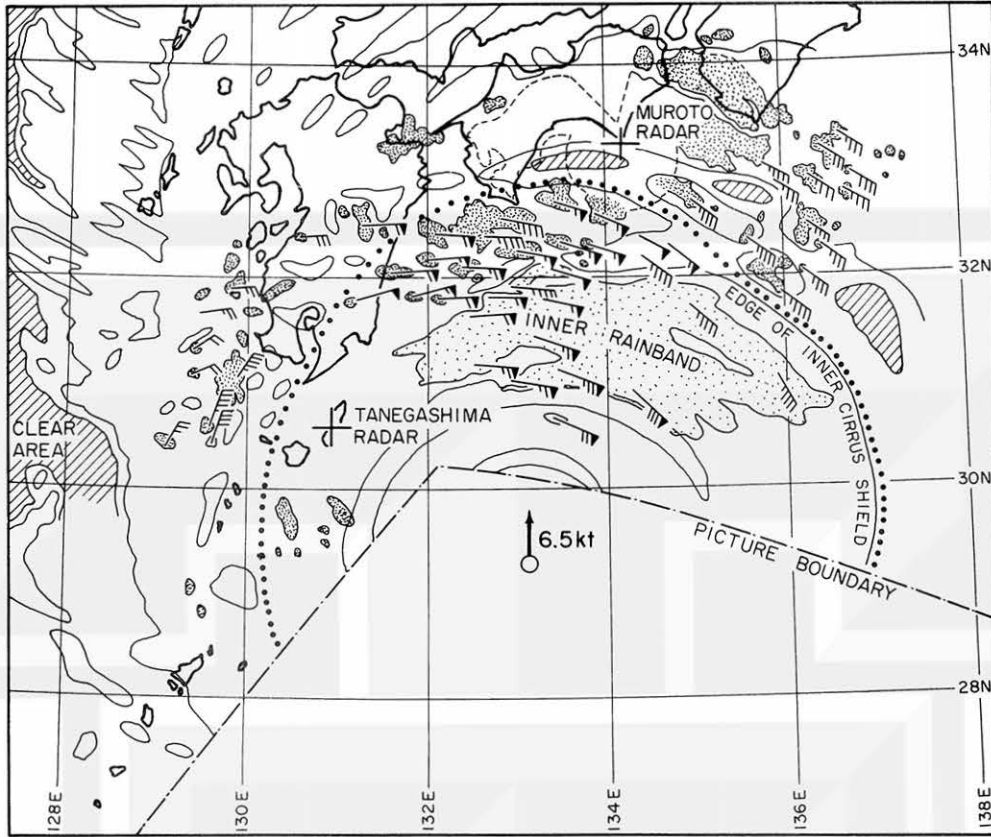


Fig. 9. Velocities of echoes forming outer and inner rainbands determined within a few minutes of the exposure time of Fig. 3, 0451 GMT, Aug. 8, 1963.

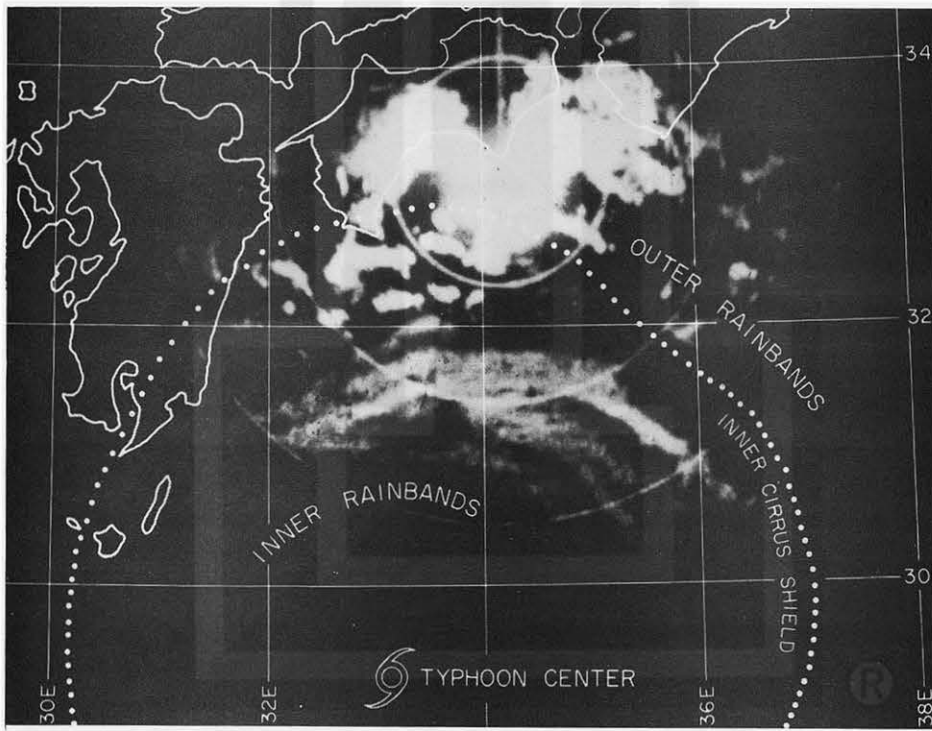


Fig. 10. Radar picture from Muroto, Shikoku taken within a few minutes of the exposure time of Fig. 3. Echoes forming the inner rainbands are more or less continuous while those in the outer rainbands are cellular, somewhat like those seen in squall lines.

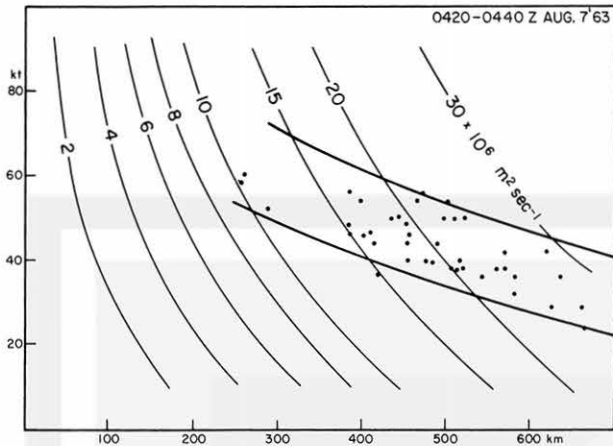


Fig. 11. Tangential velocities of radar echoes plotted against the distance from the storm center. The upper diagram was obtained from echo velocities in Fig. 7 and the lower, from Fig. 9. The isolines of absolute angular momentum in the diagrams show that the momentum of echoes forming inner rainbands (open circles) is much smaller than those forming outer rainbands (black dots). Heavy lines represent both upper and lower limits of scattered points.

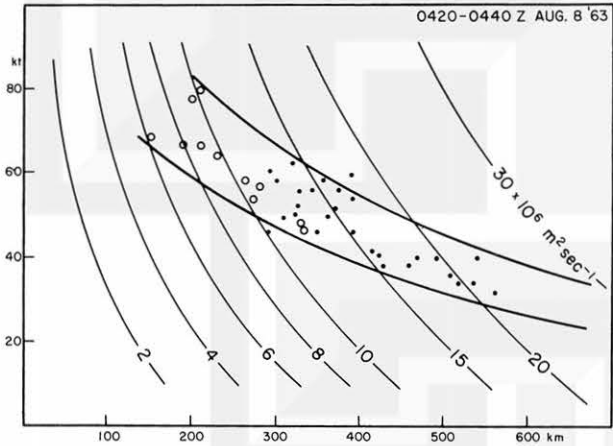
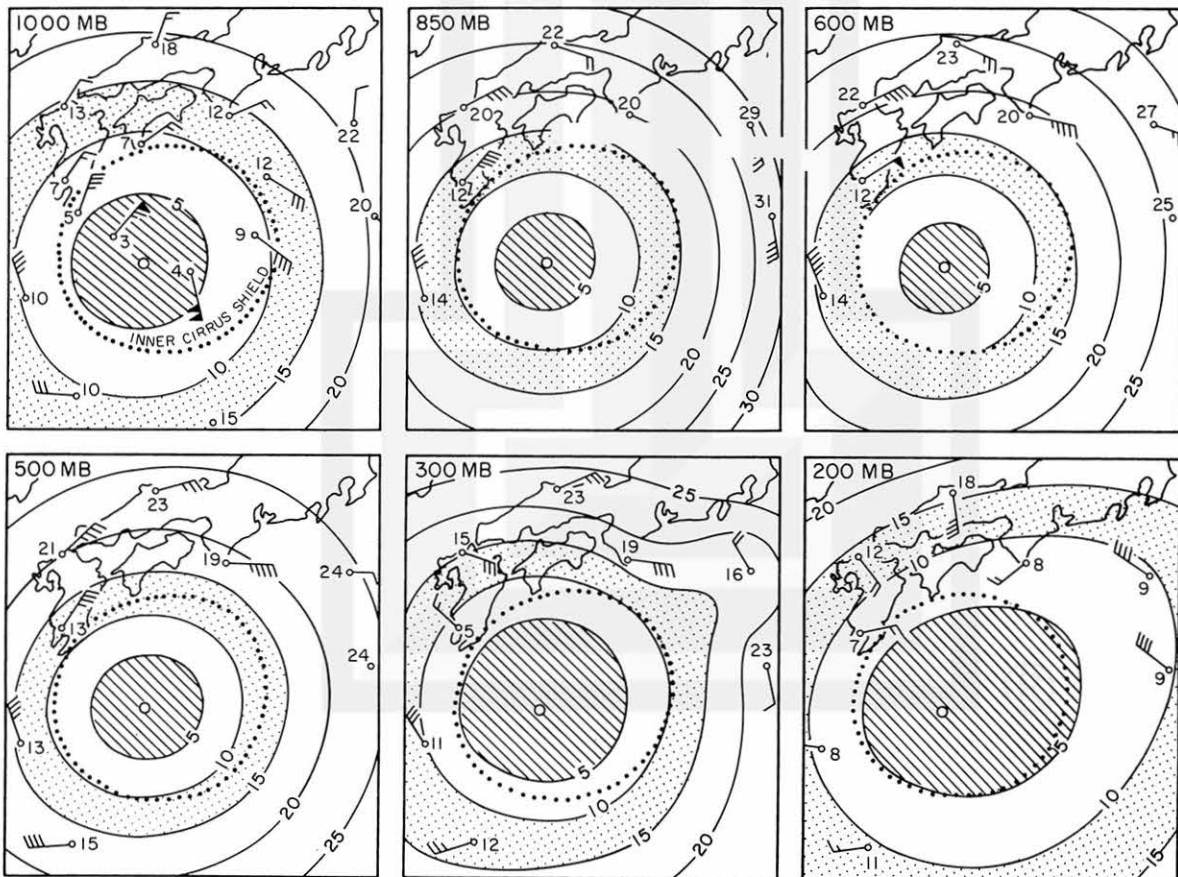


Fig. 12. Distribution of absolute angular momentum of the air at six pressure surfaces inside Typhoon Bess at 00 GMT, Aug. 8, 1963. Numbers indicated next to each wind symbol are the absolute angular momentum in $10^6 \text{ m}^2 \text{ sec}^{-1}$. Stippled and hatched areas are the regions of absolute angular momentum between 5 and 10 and less than $5 \times 10^6 \text{ m}^2 \text{ sec}^{-1}$. Dotted lines represent the boundary of inner cirrus shield.



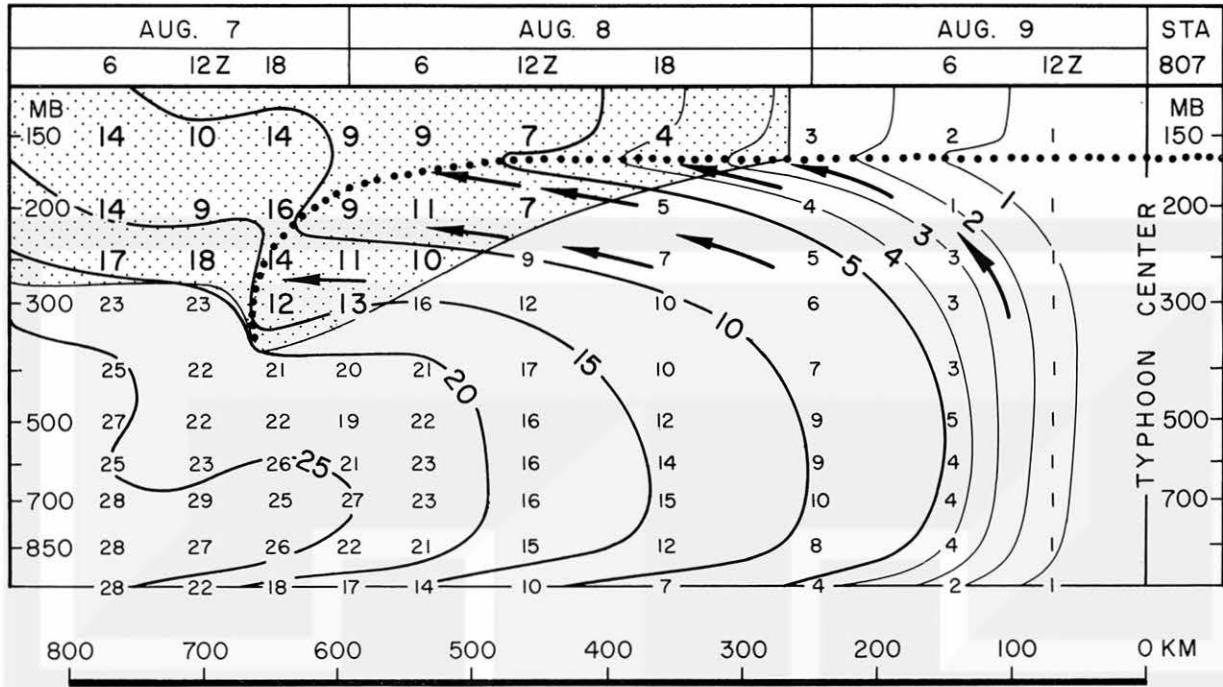


Fig. 13. Time section of the absolute angular momentum at Fukuoka (807), Kyushu during the approaching period of Typhoon Bess, which was weakening. The bottom scale indicates the distance of the storm center from Fukuoka. Numbers and contours represent absolute angular momentum in $10^6 \text{m}^2 \text{sec}^{-1}$. Region of negative relative angular momentum or that of anticyclonic angular momentum viewed from terrestrial coordinate is stippled. Arrows indicate the direction of circulation if the conservation of absolute angular momentum is assumed.

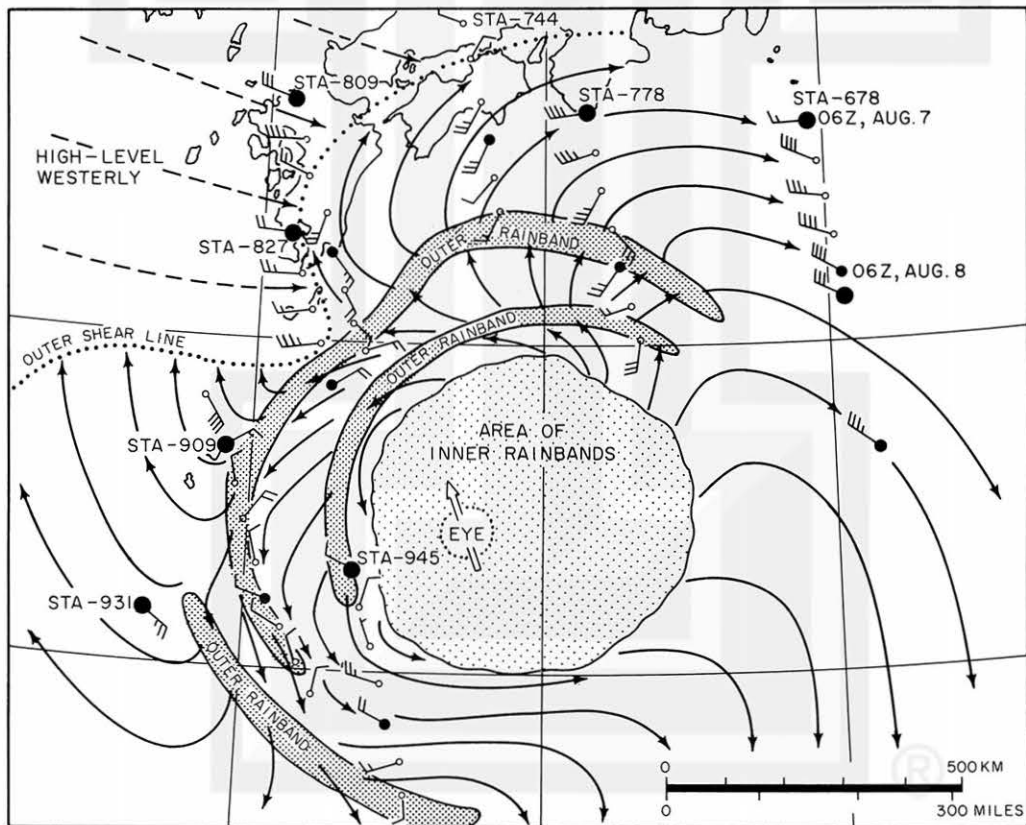


Fig. 14. Model diagram of a typhoon outflow which receives both mass and absolute angular momentum solely from mesoscale penetrative convective systems. In the mathematical treatment both positive and negative vertical velocities are included in the outflow calculation.

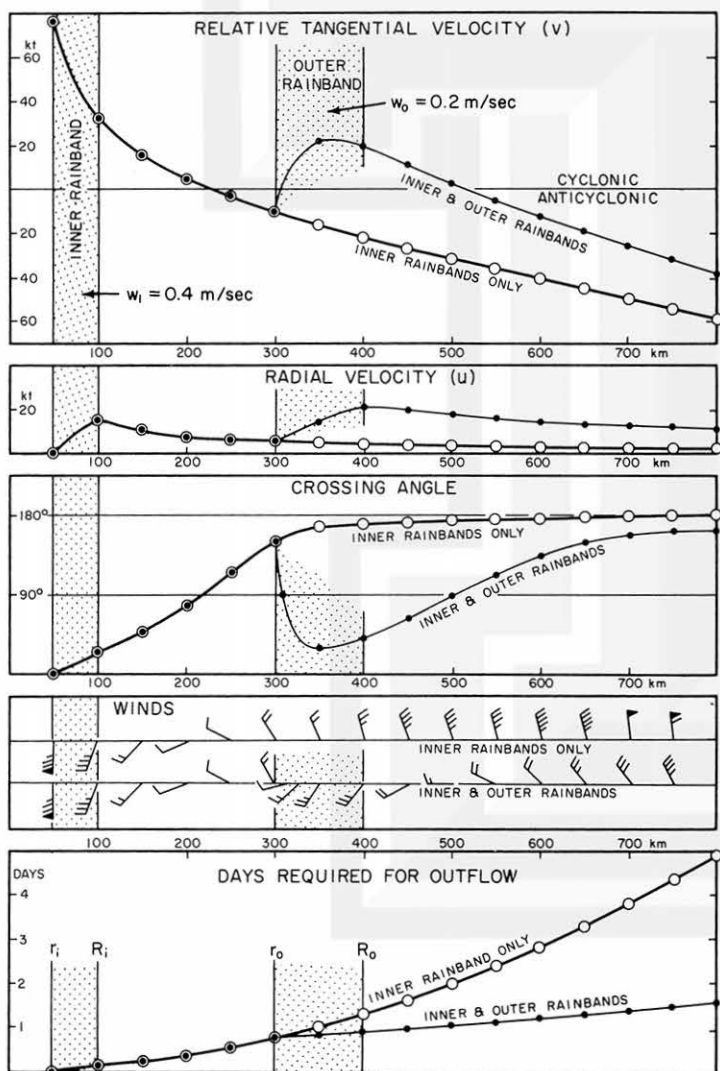
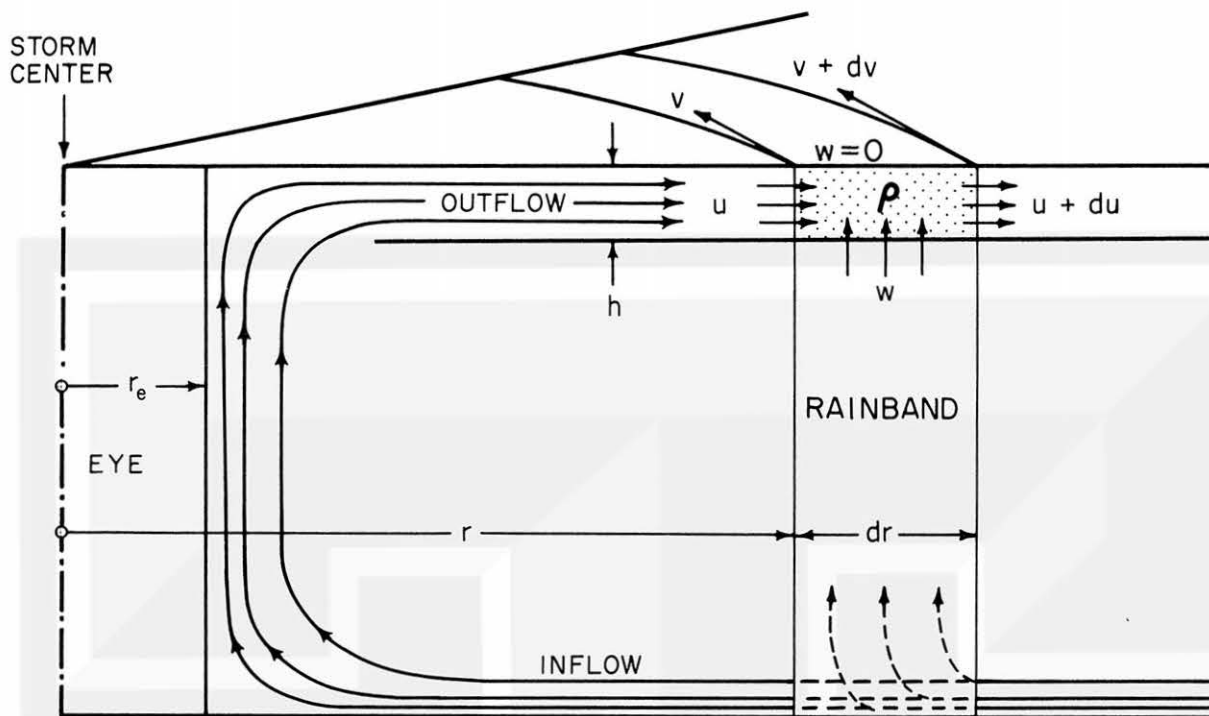


Fig. 15. Mesoscale outflow patterns obtained by converting time changes of 200-mb winds at each station into space distributions by plotting them along vectors parallel but opposite to the velocity of Typhoon Bess. Winds during about a 24-hr period ending 06Z, Aug. 8, 1963 were used in drawing streamlines.

Fig. 16. Radial distributions of relative tangential velocity, radial velocity, crossing angle, and wind velocity computed from Eqs. (6) through (9), (12), (13), (15), (19), and (25). Cases with and without outer rainbands are presented in the figure. Note the generation of significant cyclonic wind shear along the inside edge of the outer rainband.

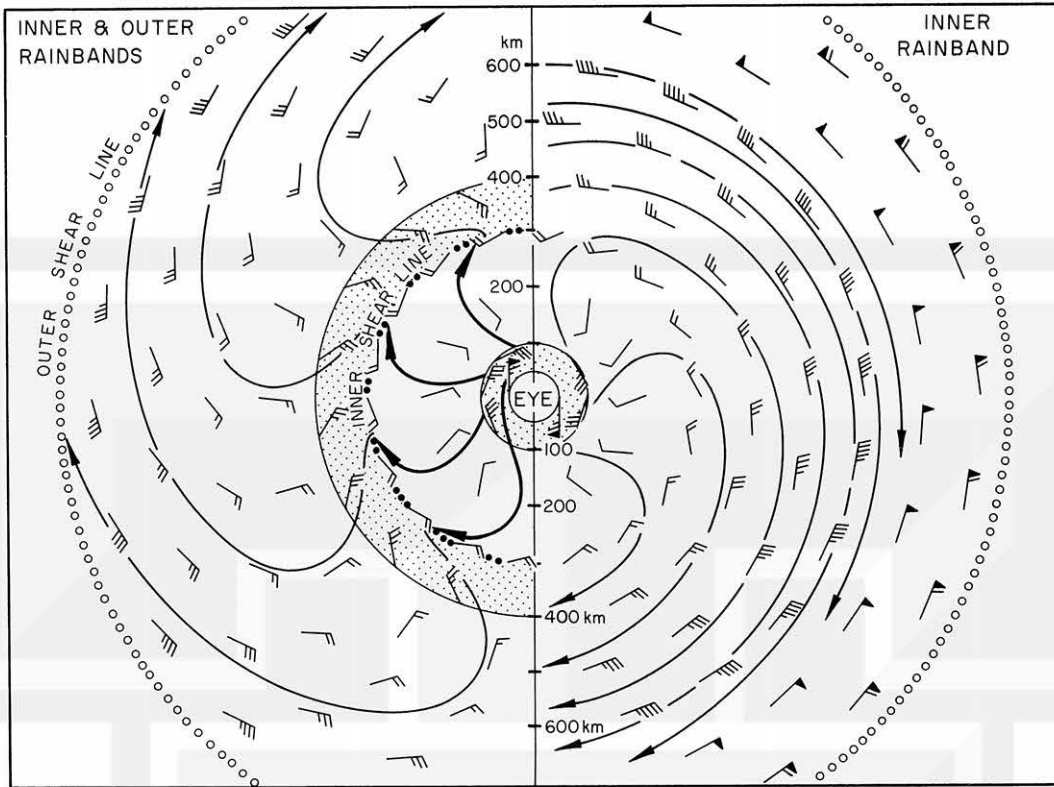


Fig. 17. Two-dimensional distribution of outflow winds for a model typhoon with an inner rainband between 50 and 100 km from the center (right half). The left half represents a model with an outer rainband in addition to the inner. A shear line circling the inner cirrus shield is seen when the typhoon is accompanied by a distinct inner and outer rainband.

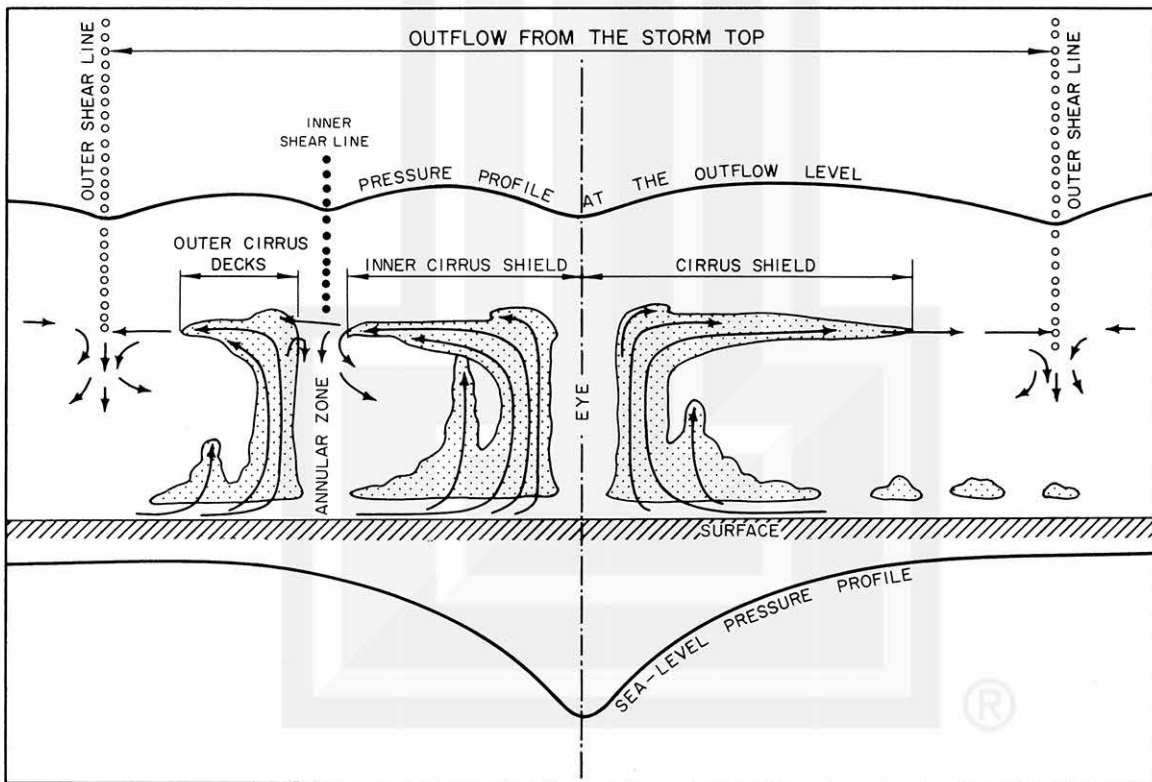


Fig. 18. A schematical cross-section of model typhoons of Fig. 17 in which two models are shown on both sides of a center line. It should be pointed out that the pressure along both outer and inner shear lines is slightly low, thus creating convergent outflow winds which subside a certain depth.

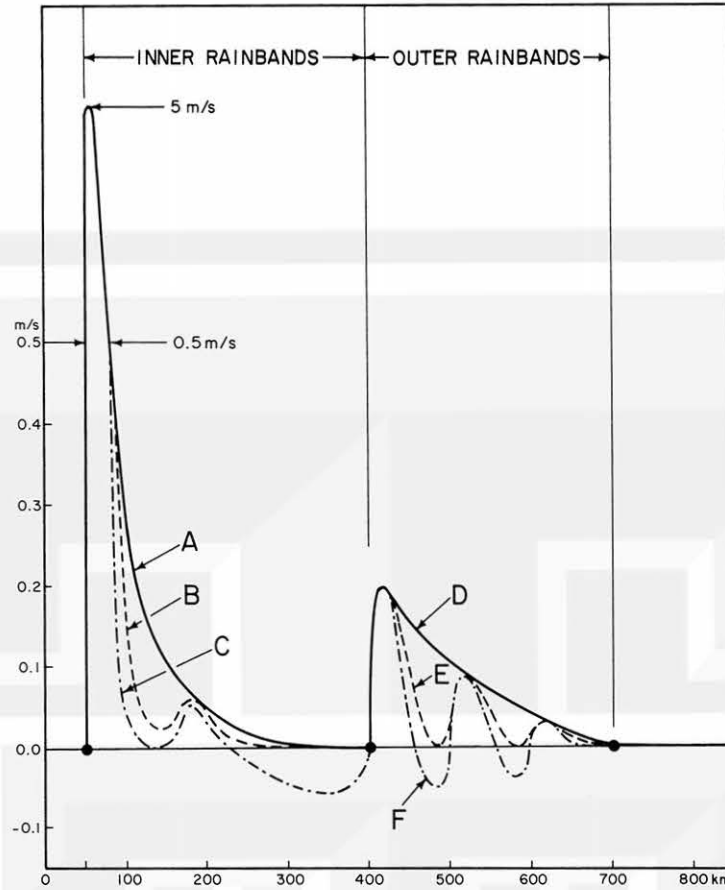


Fig. 19. Generalized distributions of the vertical velocities inside inner and outer rainbands. The distributions A, B, C for the inner and D, E, F for the outer rainbands permit us to calculate outflow winds of 15 model typhoons. Both C and F include downward motion at the outflow level.

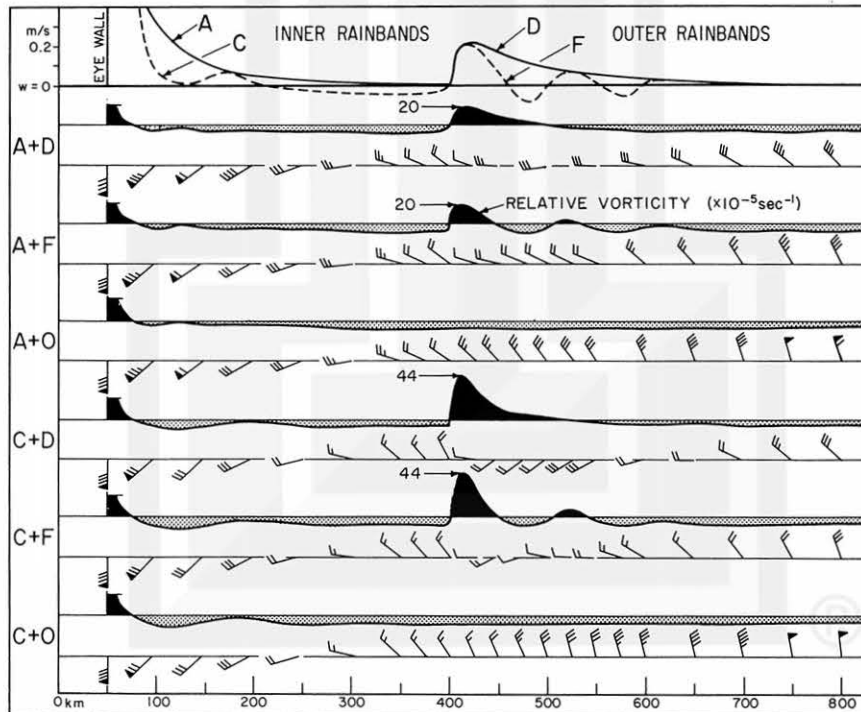


Fig. 20. Radial distribution of winds and relative vorticity at the outflow level of model typhoons. Vertical velocities at the base of the outflow layer are given as combinations of A, C, D, and F shown at the top of the figure. Positive and negative relative vorticities are shown by painted and stippled areas, respectively.

MESOMETEOROLOGY PROJECT - - - RESEARCH PAPERS

(Continued from front cover)

42. A Study of Factors Contributing to Dissipation of Energy in a Developing Cumulonimbus - Rodger A. Brown and Tetsuya Fujita
43. A Program for Computer Gridding of Satellite Photographs for Mesoscale Research - William D. Bonner
44. Comparison of Grassland Surface Temperatures Measured by TIROS VII and Airborne Radiometers under Clear Sky and Cirriform Cloud Conditions - Ronald M. Reap
45. Death Valley Temperature Analysis Utilizing Nimbus I Infrared Data and Ground-Based Measurements - Ronald M. Reap and Tetsuya Fujita
46. On the "Thunderstorm - High Controversy" - Rodger A. Brown
47. Application of Precise Fujita Method on Nimbus I Photo Gridding - Lt. Cmd. Ruben Nasta
48. A Proposed Method of Estimating Cloud-top Temperature, Cloud Cover, and Emissivity and Whiteness of Clouds from Short- and Long-wave Radiation Data Obtained by TIROS Scanning Radiometers - T. Fujita and H. Grandoso
49. Aerial Survey of the Palm Sunday Tornadoes of April 11, 1965 - Tetsuya Fujita
50. Early Stage of Tornado Development as Revealed by Satellite Photographs - Tetsuya Fujita
51. Features and Motions of Radar Echoes on Palm Sunday, 1965 - D. L. Bradbury and Tetsuya Fujita
52. Stability and Differential Advection Associated with Tornado Development - Tetsuya Fujita and Dorothy L. Bradbury
53. Estimated Wind Speeds of the Palm Sunday Tornadoes - Tetsuya Fujita
54. On the Determination of Exchange Coefficients: Part II - Rotating and Nonrotating Convective Currents - Rodger A. Brown
55. Satellite Meteorological Study of Evaporation and Cloud Formation over the Western Pacific under the Influence of the Winter Monsoon - K. Tsuchiya and T. Fujita
56. A Proposed Mechanism of Snowstorm Mesojet over Japan under the Influence of the Winter Monsoon - T. Fujita and K. Tsuchiya
57. Some Effects of Lake Michigan upon Squall Lines and Summertime Convection - Walter A. Lyons
58. Angular Dependence of Reflection from Stratiform Clouds as Measured by TIROS IV Scanning Radiometers - A. Rabbe
59. Use of Wet-beam Doppler Winds in the Determination of the Vertical Velocity of Raindrops inside Hurricane Rainbands - T. Fujita, P. Black and A. Loesch

